energy&fuels

Article

Cite This: Energy Fuels 2019, 33, 3077−3088

pubs.acs.org/EF

Swelling Mechanism of Core−Shell Polymeric Nanoparticles and Their Application in Enhanced Oil Recovery for Low-Permeability Reservoirs

Yunqian Long,*[,†] Xiaohe Huang,*[,‡] Ying Gao,[§] Liqiao Chen,[†] Fuquan Song,[‡] and Huiqiu Zhang[†]

[†]Institute of Innovation & Application and [‡]School of Petrochemical & Energy Engineering, Zhejiang Ocean University, Zhoushan 316022, China

[§]Institute of Mechanics, Chinese Academy of Science, Beijing 100190, China

ABSTRACT: Nanotechnology provides potential benefits for enhanced oil recovery (EOR) in low-permeability reservoirs. In this paper, SiO_2/P(MBAAm-*co*-AM) composite nanoparticles were prepared using the distillation precipitation polymerization method. Scanning electron microscopy, transmission electron microscopy, Fourier transform infrared spectroscopy, and thermogravimetric analysis were employed to characterize the morphology and microstructure of nanoparticles. The swelling behavior of polymeric nanoparticles in brine was investigated to evaluate the effect of salinity and temperature. Kinetic and thermodynamic analyses were employed to reveal the swelling mechanism. Displacement experiments were performed to investigate their performance in EOR in low-permeability reservoirs. The results show that the swelling ratio of SiO_2/P(MBAAm-*co*-AM) composite nanoparticles is higher at low salinity and high temperature, which can be explained by the Flory theory. The swelling process is spontaneous and endothermic, being controlled by physical adsorption involving the diffusion of water molecules, which complies with the first-order kinetics model. The suspension of SiO_2/P(MBAAm-*co*-AM) composite nanoparticles can improve incremental oil recovery from 10.28 to 21.97% with an increase of the swelled particle size from 580 to 1160 nm. It is feasible that core−shell polymeric nanoparticles can be used for EOR in low-permeability reservoirs.

1. INTRODUCTION

Low-permeability reservoirs are important oil reserves that could be explored and developed to meet the demand for energy in China. Thus far, most low-permeability reservoirs have been developed by waterflood.[1−4] Low-permeability reservoirs have small pore size and complex structure, which results in high water injection pressure and low oil recovery. Particularly, serious water channeling occurs in low-permeability reservoirs in the middle and late stages of waterflooding development.[5−8] Currently, the conventional chemical flooding technologies successfully applied in medium- and high-permeability reservoirs, including polymer flooding,[9] binary compound flooding,[10] and ternary compound flooding,[11] cannot be directly transplanted in low-permeability reservoirs because of high injection pressure, which makes it very difficult to improve oil recovery in low-permeability reservoirs.

Recently, nanotechnology has emerged as an alternative to improve oil recovery in low-permeability reservoirs. Nanofluid flooding, a novel technology of enhanced oil recovery (EOR) involving the injection of a nanoparticle suspension, has been widely tested over the past decade.[12−15] Some inorganic nanoparticles, including SiO_2,[16] ZrO_2,[17] NiO,[17] TiO_2,[18] and Al_2O_3,[19] have been widely investigated for their applications as nanofluids for the purpose of EOR. The mechanism for EOR using inorganic nanoparticles in low-permeability reservoirs appears to be wettability alteration of the flow passage, which decreases the water injection pressure. Al-Anssari et al.,[20] Hendraningrat et al.,[21] Radnia et al.,[22] and Bagherpour et al.[23] confirmed that it was beneficial to improve oil recovery for wettability alteration of flow passage by inorganic nanoparticles.

Although highly efficient for improving the EOR water injection, water channeling in low-permeability reservoirs cannot be easily controlled when using inorganic nanoparticles. Therefore, core−shell polymeric nanoparticles have been extensively studied for their applications as a new class of materials termed polymeric nanofluids with the aim to the control the profile to improve oil recovery in low-permeability reservoirs.[24−28] The core−shell polymeric nanoparticles are synthesized by the induction of polymer on the surface of inorganic nanoparticles, with a core of inorganic nanoparticle and a shell consisting of an organic polymer. These polymeric nanoparticles are hydrophilic and can swell from the original nano size or submicron size to micron size in water. When the swollen polymeric nanoparticles are injected into the reservoirs, they can produce plugging at the throats to change the flow direction of water, and a new bypass is formed to promote the sweep efficiency of the injected water. Water channeling in low-permeability reservoirs can be well controlled. As compared with individual polymer or nanoparticles, the core−shell polymeric nanoparticles have high-performance characteristics, improved thermal properties, and salinity-tolerant behaviors because of the strong bonding force between inorganic nanoparticles and polymers.

Wang et al. prepared a kind of swollen polymeric nanoparticles that could swell from 50 nm to several microns in water and resisted high salt concentration and high temperature.[29] Hu et al. prepared a novel aqueous hydrolyzed

Received: January 14, 2019
Revised: March 20, 2019
Published: March 27, 2019

DOI: 10.1021/acs.energyfuels.9b00131
Energy Fuels 2019, 33, 3077−3088

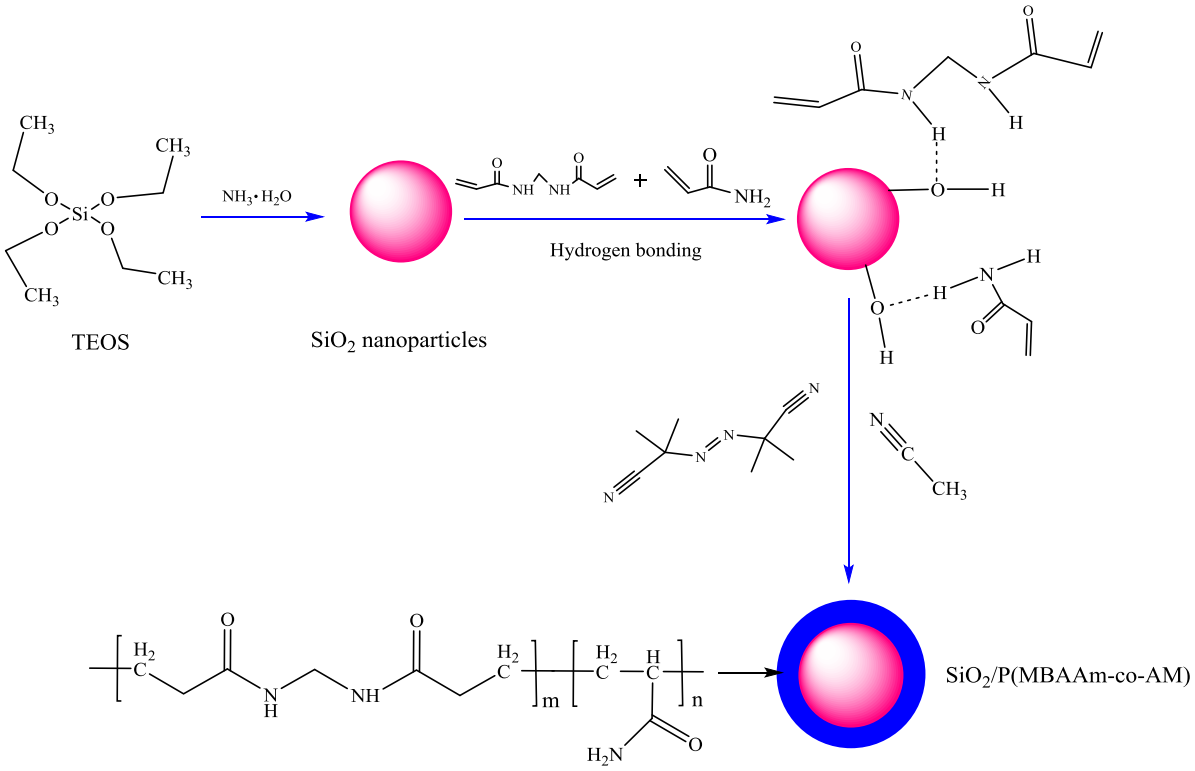

Figure 1. Schematic illustration of the synthesis of SiO_2/P(MBAAm-*co*-AM) composite nanoparticles.

polyacrylamide-based SiO_2 nanosuspension for EOR, and its rheological properties were investigated under different salinities and temperatures.[30] Zhu et al. formulated a polymer-grafted nanoparticle suspension by grafting a novel vinyltriethoxysilane-functionalized SiO_2 onto acrylamide (AM)/acrylic acid copolymer with the aim of obtaining a polymeric nanofluid with temperature and salt tolerance.[31] Alaskar et al. investigated the flow of polymeric nanoparticles through porous and fractured media and found that particle size, particle size distribution, shape, and surface charge were the main parameters affecting the transportation of polymeric nanoparticles through the porous media.[32] Liu et al. performed rheological studies on a novel core−shell polymer-grafted nanoparticle synthesized from in situ free-radical polymerization-functionalized SiO_2 nanoparticle and acrylamide-based polymer molecules.[33] However, these studies did not investigate the swelling mechanism of the core−shell polymeric nanoparticles and the influence of the swelling property on EOR.

In this study, the synthesized SiO_2/P(MBAAm-*co*-AM) composite nanoparticles were characterized to investigate their morphology and microstructure by scanning electron microscopy (SEM), transmission electron microscopy (TEM), Fourier transform infrared spectroscopy (FT-IR), and thermogravimetric analysis (TGA). Laboratory experiments investigated the swelling behavior at various salinities and temperatures. Their swelling mechanism was revealed by kinetic and thermodynamic analyses. The suspension was prepared by mixing SiO_2/P(MBAAm-*co*-AM) composite nanoparticles with water. The suspension of SiO_2/P(MBAAm-*co*-AM) was investigated for EOR in low-permeability cores by flood experiments. The objectives of this paper are to understand the swelling mechanism of SiO_2/P(MBAAm-*co*-AM) composite nanoparticles and to quantify the influence of their swelling property on the EOR in low-permeability reservoirs.

2. EXPERIMENTAL SECTION

2.1. Materials. Chemical reagents used in this work were analytical grade and mixed with deionized water in the laboratory. Tetraethyl orthosilicate (TEOS, 28.5%) was purchased from Modern Oriental Fine Chemicals Co., Ltd. (Beijing, China). Acrylamide (AM), *N*,*N*-methylene-bis-acrylamide (MBAAm), azodiisobutyronitrile (AIBN), and acetonitrile were purchased from Sinopharm Chemical Reagent Co., Ltd. (Beijing, China). Ethyl alcohol and ammonia solution (25%) were purchased from Beihua Fine Chemicals Co., Ltd. (Beijing, China).

A crude oil sample from a Daqing oil reservoir was used for displacement experiments. At the reservoir temperature of 45 °C, the crude oil had a density of 0.895 g/cm^3 and a viscosity of 15.2 mPa s. The synthetic formation water for all tests was a brine with the total dissolved solids (TDSs) of 5380 mg/L. Cores 5.0 cm in length and 2.5 cm in diameter were obtained from a Daqing oil reservoir.

2.2. Synthesis of Monodisperse SiO_2 Nanoparticles. The monodisperse SiO_2 nanoparticles were prepared using a Stöber process.[34] In a 250 mL conical flask, 11.2 mL TEOS was added to the premixed ethyl alcohol solution (84.1 mL) containing 17.1 mL deionized water and then 4.76 mL ammonia solution was mixed under continuous magnetic stirring (130 rpm). After being stirred for 6 h, the SiO_2 nanoparticles were centrifuged with 8000 rpm and washed several times with ethanol. The samples were dried in a vacuum at 70 °C for 8 h.

2.3. Synthesis of SiO_2/P(MBAAm-*co*-AM) Composite Nanoparticles. SiO_2/P(MBAAm-*co*-AM) composite nanoparticles were synthesized by distillation precipitation polymerization.[35] The as-prepared SiO_2 nanoparticles (0.5 g), MBAAm (0.2 g), and AM (0.5 g) were added to the acetonitrile solution (40 mL) in a 250 mL three-neck flask connected with a reflux condenser and sonicated for 10 min (100 Hz) at room temperature. Then, AIBN (0.1 g) was added to the above mixture and sonicated for 5 min (100 Hz). The temperature of the reaction solution was increased from room temperature to 90 °C

DOI: 10.1021/acs.energyfuels.9b00131
Energy Fuels 2019, 33, 3077−3088

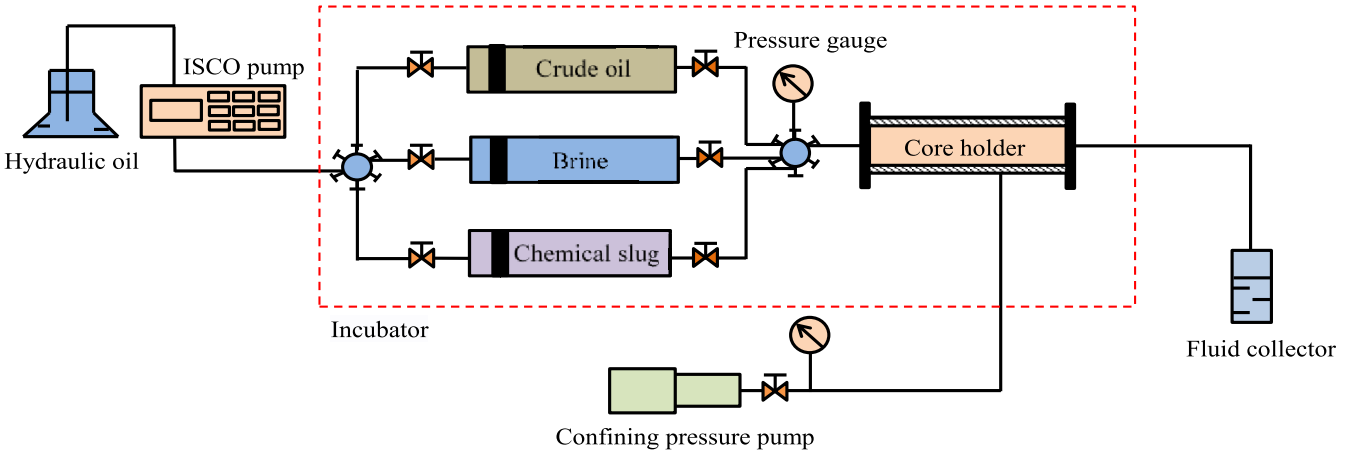

Figure 2. Schematic of the experimental setup.

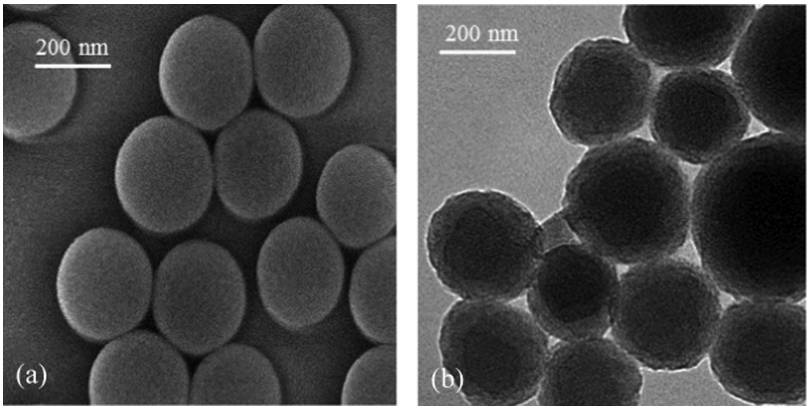

Figure 3. SEM image of SiO_2 nanoparticles (a) and TEM image of SiO_2/P(MBAAm-*co*-AM) composite nanoparticles (b).

in 15 min by using an oil bath pan and reacted at 90 °C for 15 min. After that, the mixture was heated to 115 °C and distilled for 90 min with a reflux ratio of 2 until all solvents had been distilled out. After being dissolved in ethyl alcohol, the products were sonicated for 10 min, centrifuged at 10 000 rpm for 5 min, and washed several times with deionized water to remove unreactive ingredients and solvents. Finally, SiO_2/P(MBAAm-*co*-AM) composite nanoparticles were obtained after being vacuum dried at 50 °C for 12 h. The schematic illustration of the synthesis of SiO_2/P(MBAAm-*co*-AM) composite nanoparticles is shown in Figure 1.

2.4. Characterization of SiO_2 and SiO_2/P(MBAAm-*co*-AM) Composite Nanoparticles. The Fourier transform infrared (FT-IR) spectra were recorded on a Nicolet Nexus 670 FT-IR spectrometer in the region of 4000−400 cm^{-1}. The morphological characteristics of SiO_2 and SiO_2/P(MBAAm-*co*-AM) composite nanoparticles were detected by using a Hitachi S-4500 scanning electron microscope and a JEM-200CX transmission electron microscope, respectively. The thermogravimetric analysis was performed on a SDTQ600 thermogravimetric analyzer with a heating rate of 10 °C/min under nitrogen atmosphere. The particle size distributions of these nanoparticles were determined on a Mastersizer 2000 laser particle size analyzer.

2.5. Swelling Experiments. SiO_2/P(MBAAm-*co*-AM) composite nanoparticles could not dissolve in water to form a solution but were mixed with water to form a suspension. When mixed with water, SiO_2/P(MBAAm-*co*-AM) composite nanoparticles could absorb a lot of water to swell, with their diameters increasing from original nano or submicron to micron size, because of hydrogen bonds formed with water molecules. A laser particle size analyzer was employed to study the swelling behavior of SiO_2/P(MBAAm-*co*-AM) composite nanoparticles as a function of time in various salinity and temperature conditions. Medium diameter of polymeric nanoparticles measured by a laser particle size analyzer was considered as average particle diameter. The swelling property was described and monitored by the swelling ratio defined as follows

$$Q = \frac{D_2 - D_1}{D_1} \quad (1)$$

where Q is the swelling ratio, D_2 is the average particle diameter of swollen polymeric nanoparticles at each time interval, μm, and D_1 is the average particle diameter of the initial dry composite nanoparticles, μm.

2.6. Core-Flooding Experiments. The experimental setup used for core-flooding experiments is shown in Figure 2, which consisted of a hydrostatic core holder (Haian Petroleum Scientific Research Instrument Co., Ltd., China), a pump to maintain the confining pressure, a displacement pump (Teledyne Isco) for the flooding agent, and a fluid accumulator for holding the collected oil sample, brine, and chemical slug. Before commencing flooding experiments, the core samples were properly cleaned and dried for 72 h at 150 °C. Their porosity was measured using weight method, and permeability measurement was conducted using the Darcy's law. Other parameters of the Darcy's equation, such as pressure and viscosity, were determined using a pressure gauge and rheometer, respectively.

In each flood test, the core was first saturated with brine, then mounted in hydrostatic core holders at a confining pressure of 3 MPa, and finally flooded with crude oil at a constant injection rate of 0.2 mL/min until the condition of irreducible water saturation was achieved in core. Flood experiments were carried out at 45 °C. The initial oil saturation was determined by material balance calculations from the volume of brine produced. The core was aged for 48 h to achieve the wettability state at 45 °C. After that, the core sample was flooded with brine at a flow rate of 0.2 mL/min until the water cut was about 98%. At this stage, a large amount of crude oil was

DOI: 10.1021/acs.energyfuels.9b00131
Energy Fuels 2019, 33, 3077−3088

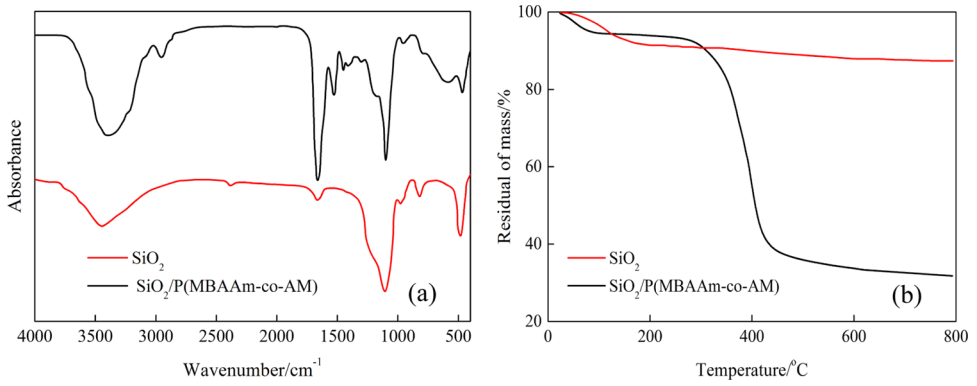

Figure 4. FT-IR spectra (a) and TGA curves (b) of SiO_2 nanoparticles and SiO_2/P(MBAAm-*co*-AM) composite nanoparticles.

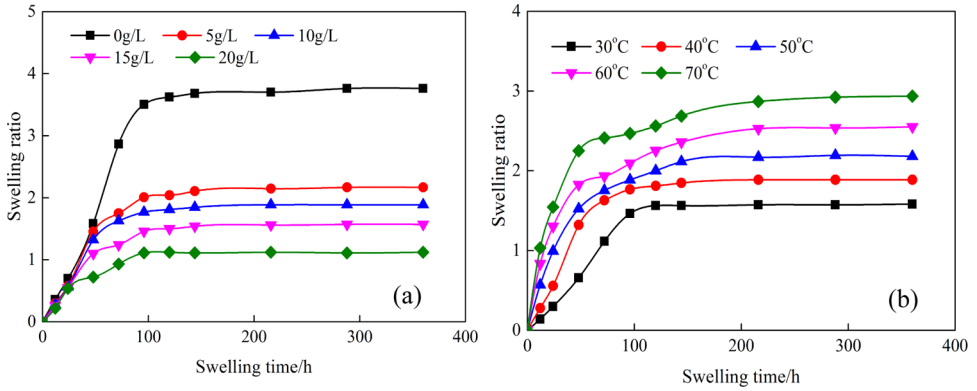

Figure 5. Effects of salinity ((a), TDS = 0−20 g/L, T = 40 °C) and temperature ((b), TDS = 10 g/L, T = 30−70 °C) on swelling behavior of SiO_2/P(MBAAm-*co*-AM) composite nanoparticles.

recovered, leaving some residual crude oil in the core. The residual crude oil trapped in the core was recovered using 0.5 pore volume (PV) of suspension, which was prepared by mixing SiO_2/P(MBAAm-*co*-AM) composite nanoparticles (1.5 g) with water (1 L), and injecting at a constant injection rate of 0.2 mL/min, followed by an extended waterflooding at the same flow rate until the oil production stopped. The recovered crude oil and brine were collected in a fluid collector, and the injection pressure data were recorded.

3. RESULTS

3.1. Morphology Characterization of SiO_2 and SiO_2/P(MBAAm-*co*-AM) Composite Nanoparticles. Figure 3a shows the SEM morphologies of SiO_2 nanoparticles. Pure SiO_2 nanoparticles are spherical with diameters ranging from 220 to 260 nm. The TEM micrographs of SiO_2/P(MBAAm-*co*-AM) composite nanoparticles are shown in Figure 3b. From the TEM image of SiO_2/P(MBAAm-*co*-AM) composite nanoparticles, it is clear that the spherical morphology remains intact. Moreover, the TEM image indicates that SiO_2/P(MBAAm-*co*-AM) composite nanoparticles are composed of a SiO_2 core and a shell of polymer. The sizes of SiO_2/P(MBAAm-*co*-AM) composite nanoparticles are in the range of 340−460 nm in diameter. The thickness of the polymer layer is calculated to be between 60 and 100 nm. The results indicate that polymer is present on the surface of SiO_2 nanoparticles, and SiO_2/P(MBAAm-*co*-AM) composite nanoparticles were successfully prepared.

3.2. Microstructure Characterization of SiO_2 and SiO_2/P(MBAAm-*co*-AM) Composite Nanoparticles. The FT-IR spectra of SiO_2 nanoparticles and SiO_2/P(MBAAm-*co*-AM) polymeric nanoparticles are shown in Figure 4a. The adsorption peaks at 3415, 1099, 957, 806, and 464 cm^{-1} are the characteristic peaks of SiO_2.[36] In the spectrum of SiO_2/P(MBAAm-*co*-AM), the structure of SiO_2/P(MBAAm-*co*-AM) is illustrated in Figure 4a. The adsorption peaks at 1099 and 949 cm^{-1} are the characteristic peaks of SiO_2 that are associated with the symmetric stretching vibration of Si−O−Si bond and the stretching vibration of the Si−OH bond.[37] The peaks at 3399 and 1662 cm^{-1} are likely attributed to the stretching vibration of the N−H bond and the C═O bond in the amide group, respectively.[38] The peaks at 2930 and 1451 cm^{-1} may be attributed to the stretching vibration of the C−H bond and the bending vibration of the C−H bond in the saturated alkyl group.[39] Consequently, these results provide further evidence for the successful preparation of the SiO_2/P(MBAAm-*co*-AM) composite nanoparticles.

The TGA analysis was carried out to evaluate the thermostability of the synthesized nanoparticle samples. The TGA curves of SiO_2 nanoparticles and SiO_2/P(MBAAm-*co*-AM) composite nanoparticles are shown in Figure 4b. The weight losses of SiO_2 nanoparticles and SiO_2/P(MBAAm-*co*-AM) composite nanoparticles before 185 °C are attributed to the loss of adsorbed water in the samples.[40] SiO_2 nanoparticles show a small degradation with the weight losses of 4.26% between 185 and 800 °C. The TGA curve of SiO_2/P(MBAAm-*co*-AM) composite nanoparticles shows three distinct steps. The first step occurs from ambient temperature to 185 °C, with a weight loss of 6.02%, which is because of the physical loss of adsorbed water. The second step illustrates a weight loss of 56.67% between 185 and 464 °C, which is associated with the loss of polymers caused by the pyrolysis of

DOI: 10.1021/acs.energyfuels.9b00131
Energy Fuels 2019, 33, 3077−3088

Table 1. Results of Core-Flooding Tests for EOR

test	permeability (10^{-3} μm^2)	porosity (%)	median particle size (nm)	initial oil saturation (%)	oil recovery of waterflood (%)	final oil recovery (%)	incremental oil recovery (%)
1	7.15	22.02	580	64.06	52.16	62.44	10.28
2	5.64	21.52	840	65.38	45.34	59.39	14.05
3	6.87	20.91	1050	62.56	42.22	58.92	16.70
4	6.29	20.33	1160	63.97	40.32	62.29	21.97

carbon chains. The third step corresponds to a weight loss of 6.52% between 464 and 800 °C, which is ascribed to dehydroxylation from SiO_2. According to the total loss of SiO_2/P(MBAAm-*co*-AM) composite nanoparticles in the TGA curve, about 56.67% of P(MBAAm-*co*-AM) was grafted on the surface of SiO_2 and the residue was about 30.79% of SiO_2. These results further demonstrate that P(MBAAm-*co*-AM) was successfully grafted on the surface of SiO_2.

3.3. Swelling Properties of SiO_2/P(MBAAm-*co*-AM) Composite Nanoparticles. The swelling experiments in aqueous solution were carried out to investigate the effects of salinity and temperature on the swelling behavior of SiO_2/P(MBAAm-*co*-AM) composite nanoparticles. The plots of the swelling ratios of SiO_2/P(MBAAm-*co*-AM) composite nanoparticles versus the swelling time at salinity ranging from 0 to 20 g/L are shown in Figure 5a. The swelling ratios of SiO_2/P(MBAAm-*co*-AM) composite nanoparticles at various salinities rapidly increase at the initial stage and then slowly increase until the swelling reaches an equilibrium. One possible reason is that lots of $-CONH_2$ groups on the surfaces of SiO_2/P(MBAAm-*co*-AM) composite nanoparticles are ionized in a short time at the initial stage. However, in the latter stage, there are few $-CONH_2$ groups on the surfaces of SiO_2/P(MBAAm-*co*-AM) composite nanoparticles with a slow increase of the swelling ratio. In addition, increasing salinity has a large influence on the swelling ratio of SiO_2/P(MBAAm-*co*-AM) composite nanoparticles, in that it can decrease the swelling ratio. It can be explained that in a high-salinity solution, a high ionic concentration can reduce the stretching of polymer molecular chains through weakening the electrostatic repulsion among the anionic polymers on the surfaces of SiO_2.[41]

The plots of swelling ratios of SiO_2/P(MBAAm-*co*-AM) composite nanoparticles versus swelling time at temperature ranging from 30 to 70 °C are shown in Figure 5b. Similarly, the swelling ratios of SiO_2/P(MBAAm-*co*-AM) composite nanoparticles at various temperatures sharply increase at the initial stage and then slowly increase until their swelling reaches an equilibrium. Furthermore, increasing temperature also has an effect on the swelling ratio of SiO_2/P(MBAAm-*co*-AM) composite nanoparticles, in that it can increase the swelling ratio. It may suggest that increasing the temperature can strengthen the stretching of the polymer molecular chains by enhancing the hydrolysis of the anionic polymers on the surfaces of SiO_2.[42]

3.4. Enhanced Oil Recovery by SiO_2/P(MBAAm-*co*-AM) Composite Nanoparticles. Four flooding tests were carried out using the suspension of SiO_2/P(MBAAm-*co*-AM) composite nanoparticles swollen at 45 °C for 24, 48, 72, and 120 h. The results were compared to investigate the influence of particle size on pressure drop, incremental oil recovery, and water cut. The concentrations of SiO_2/P(MBAAm-*co*-AM) composite nanoparticles in the suspension in all four tests were 1500 mg/L. Flooding tests were conducted on four cores of similar permeability and porosity, as shown in Table 1. The particle size distribution curves of SiO_2/P(MBAAm-*co*-AM) composite nanoparticles at different swelling times are shown in Figure 6. As shown in Figure 6, the height of the

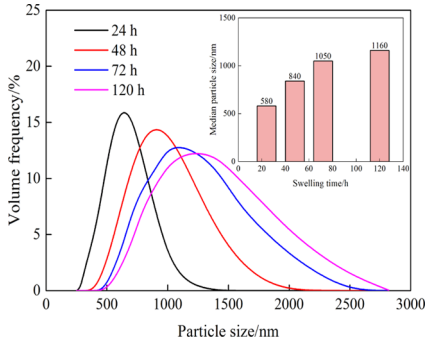

Figure 6. Particle size distribution curves of SiO_2/P(MBAAm-*co*-AM) composite nanoparticles at different swelling times.

predominant peak in volume distribution gradually becomes lower with an increase of swelling time, with a concomitant shift of particle size distributions to larger sizes. The median particle size increases from 580 to 1160 nm with an increase of swelling time ranging from 24 to 120 h.

3.4.1. Effect of Particle Size on Pressure Drop. Pressure drop was defined as pressure difference across the core inlet and outlet. The influence of particle size on pressure drop was studied by carrying out flooding experiments for SiO_2/P(MBAAm-*co*-AM) suspension with the various particle sizes shown in Table 1. The flooding pattern consisted of a waterflood, followed by a SiO_2/P(MBAAm-*co*-AM) suspension flood (0.5 PV), and then by an extended waterflood. In each test, the pressure drop was measured from the injection of water to the end of the extended waterflood as shown in Figure 7. The pressure drop remained at about 0.2 MPa during the waterflood in each test. In test 4, the pressure drop increased to

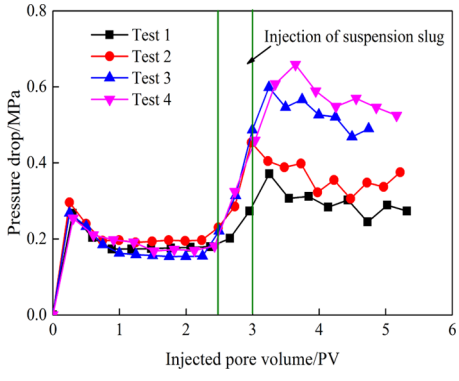

Figure 7. Effect of particle size on pressure drop as a function of injected pore volume.

DOI: 10.1021/acs.energyfuels.9b00131
Energy Fuels 2019, 33, 3077−3088

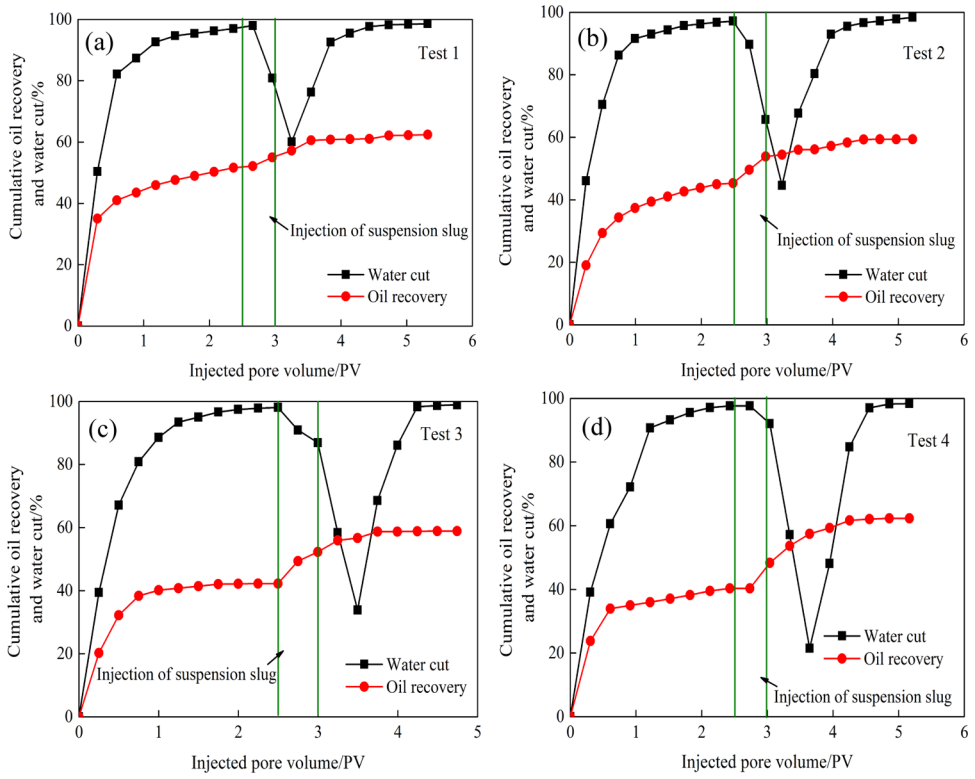

Figure 8. Production performance of the cumulative oil recovery and water cut with different median particle sizes: (a) test 1, 580 nm; (b) test 2, 840 nm; (c) test 3, 1050 nm; and (d) test 4, 1160 nm.

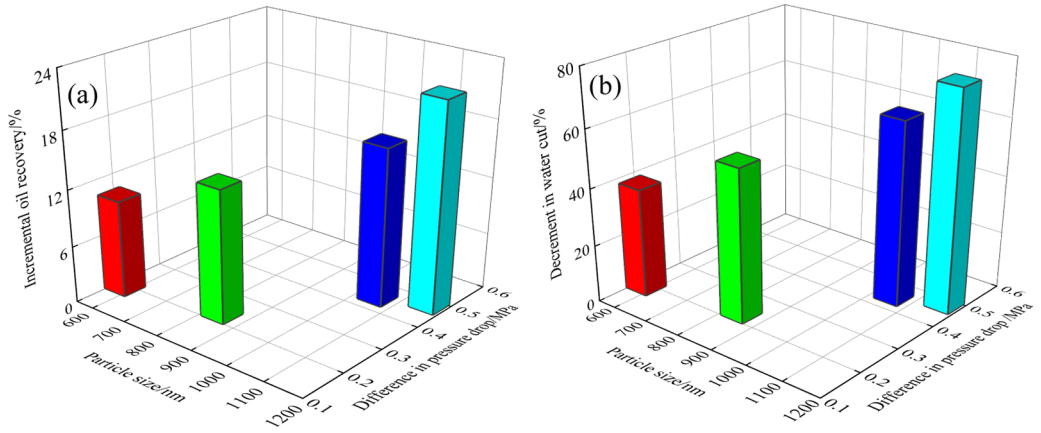

Figure 9. Effect of particle size and difference in pressure drop on production performance: (a) incremental oil recovery and (b) decrement in water cut.

0.66 MPa during the injection of SiO_2/P(MBAAm-*co*-AM) suspension with the median particle size of 1160 nm. Then, the pressure drop decreased and stabilized to about 0.55 MPa after an extended waterflood. With a decrease of the swelled particle size from 1160 to 580 nm, the pressure drop decreased from 0.66 to 0.37 MPa. The reason may be due to a decrease of particle size resulting in less flow resistance caused by SiO_2/P(MBAAm-*co*-AM) composite nanoparticles through the core, which is reflected in a drop of pressure drop. In addition, the pressure drop during the extended waterflood in each test is higher than that during the waterflood. It conveys that some SiO_2/P(MBAAm-*co*-AM) nanoparticles retained in the cores may still improve flow resistance. Moreover, pressure drop in test 4 was greater during the extended waterflood as compared to other tests. Therefore, pressure drop is directly related to the particle size of SiO_2/P(MBAAm-*co*-AM) composite nanoparticles.

3.4.2. Effect of Particle Size on EOR. The results of core-flooding experiments in relation to incremental oil recovery are recorded in Table 1. As shown in Table 1, the results indicate that SiO_2/P(MBAAm-*co*-AM) suspension can improve oil recovery efficiency after conventional waterflooding. Incremental oil recovery increases with an increase of particle size and reaches a maximum of 21.97% original oil in place (OOIP) with the largest swelled particle size of 1160 nm, which is substantially higher than those obtained for tests with smaller particle size. Thus, it can be seen that the influence of particle size on incremental oil recovery is in accordance with that on pressure drop.

DOI: 10.1021/acs.energyfuels.9b00131
Energy Fuels 2019, 33, 3077−3088

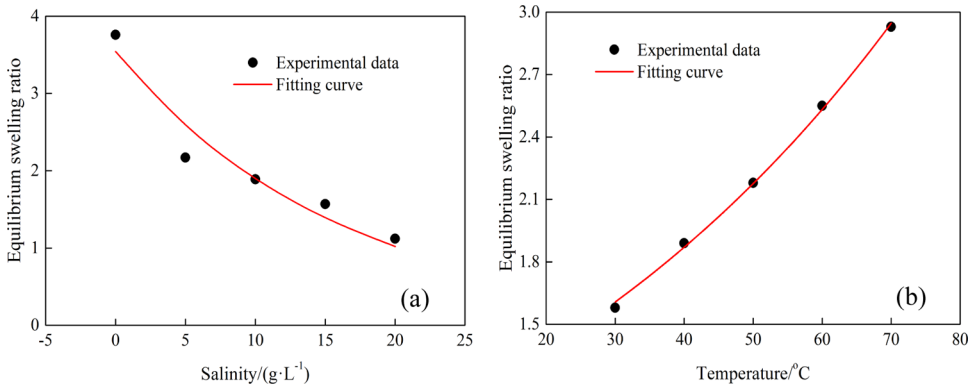

Figure 10. Effect of salinity (a) and temperature (b) on the equilibrium swelling ratio of SiO_2/P(MBAAm-*co*-AM) composite nanoparticles.

Figure 8 shows the status of cumulative oil recovery and water cut with pore volume injected for fluid in four tests. Waterflooding produces low oil recovery ranging from 40.32 to 52.16% OOIP, which can be attributed to viscosity contrast between water and crude oil resulting in low oil recovery. Water cut increases quickly above 90% during waterflooding in four tests, which indicates an early water breakthrough. SiO_2/P(MBAAm-*co*-AM) suspension flooding is commenced after water cut reaches up to 98%, followed by extended waterflooding. Water cuts reduce to 60.07, 44.56, and 33.86% in tests 1−3, respectively, and incremental oil recoveries reach 10.28, 14.05, and 16.70% OOIP, respectively. In test 4, water cut is reduced to 21.46%, lower than those in other tests, and incremental oil recovery reaches 21.97% OOIP, higher than those in other tests. The above results illustrate that decrement in water cut and incremental oil recovery increase with an increase of particle size. It can be inferred that the plugging effects of nanoparticles are enhanced at the throats with increasing particle size. Thus, crude oil can overcome capillary resistance to be migrated from small pores to improve oil recovery.

Incremental oil recovery and a decrement in water cut are plotted in Figure 9 as functions of difference in pressure drop with each particle size conditions to study the influence of difference in pressure drop between slug flooding of SiO_2/P(MBAAm-*co*-AM) suspension and waterflooding on production performance. A larger difference in pressure drop obtained with an increase of particle size can produce higher incremental oil recovery and larger decrement in water cut. An increase of the swelled particle size from 580 to 1160 nm, an increment in EOR, and a decrement in water cut increase from 10.28 to 21.97% and from 37.93 to 76.54%, respectively. This indicates that SiO_2/P(MBAAm-*co*-AM) composite nanoparticles can effectively improve oil recovery and reduce water cut.

4. DISCUSSION

4.1. Influence of Salinity and Temperature on Swelling Behavior. The effect of salinity and temperature on the swelling ratio of SiO_2/P(MBAAm-*co*-AM) composite nanoparticles can be explained by the Flory theory.[43] According to the Flory theory, the equilibrium swelling ratio (Q_e) can be calculated as follows

$$Q_e^{5/3} \approx \left[\left(\frac{i}{2V_u S^{1/2}}\right)^2 + (1/2 - x_1)/V_1\right] / \frac{V_e}{V_0} \quad (2)$$

where Q_e is the equilibrium swelling ratio, V_u is the molar volume of polymer particle, L/mol, S is the ionic strength of external electrolyte, mol/L, x_1 is the interaction parameter between polymer particle and water, V_0 is the molar volume of the nonswelling polymer particle, L/mol, V_1 is the molar volume of swelled polymer particle, L/mol, V_e is the number of effective cross-linking units for cross-linked network, i is the charge number for each structural unit, i/V_u is the charge concentration fixed on the surface of polymer particle, $(1/2 - x_1)/V_1$ is the affinity between water and polymer particle network, and V_e/V_0 is the cross-linking density of polymer particle.

According to eq 2, in electrolyte solution, the greater the electrolyte concentration, the greater is the S value and the smaller is the Q_e value of SiO_2/P(MBAAm-*co*-AM) composite nanoparticles. The Q_e value decreases with an increase of salinity. In addition, an increase of temperature will lead to further hydrolysis of amide groups in SiO_2/P(MBAAm-*co*-AM) composite nanoparticles. Hydrolysis brings about an increase of i/V_u value, and then the Q_e value of SiO_2/P(MBAAm-*co*-AM) composite nanoparticles increases as well. Further analysis reveals that i/V_u has a great value at high temperature, that is, S has a great coefficient in eq 2, which enhances the effect of S on Q_e. S has a small value at low salinity, namely, i/V_u has a great coefficient in eq 2, which enhances the effect of i/V_u on Q_e. Hence, it is evident that salinity has a greater influence on the swelling ratio at high temperature, and temperature has a greater influence on the swelling ratio at low salinity.

4.2. Equilibrium Swelling Ratio Analysis. The equilibrium swelling ratio (Q_e) is one of the most important parameters for the swelling properties of SiO_2/P(MBAAm-*co*-AM) composite nanoparticles. According to the above experimental data and eq 2, the equilibrium swelling ratio affected by salinity and temperature can be quantitatively analyzed. Figure 10a shows a plot of the equilibrium swelling ratio versus salinity. The equilibrium swelling ratio decreases gradually with increasing salinity. The plot shows that the relationship between the equilibrium swelling ratio and salinity can be approximated by the following exponential form

$$Q_e = a_C \cdot \exp(b_C \cdot C) \quad (3)$$

where a_C and b_C are the fitted parameters and C is the salinity, g/L. Under these experimental conditions, parameters a_C and b_C are 3.541 and −0.0622, respectively, by nonlinear regression analysis with correlation coefficient (R^2 = 0.911).

DOI: 10.1021/acs.energyfuels.9b00131
Energy Fuels 2019, 33, 3077−3088

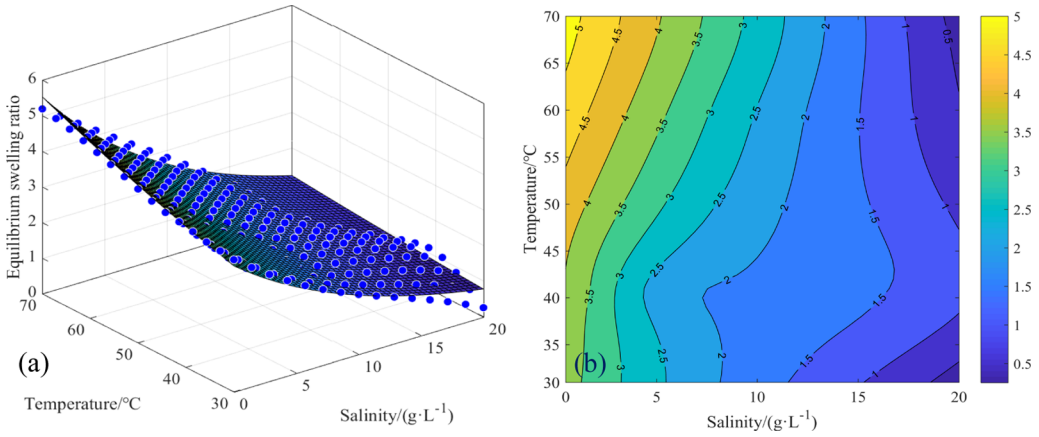

Figure 11. Fitted surface of the equilibrium swelling ratio versus salinity and temperature (a) and isograms of the equilibrium swelling ratio of SiO_2/P(MBAAm-*co*-AM) composite nanoparticles (b).

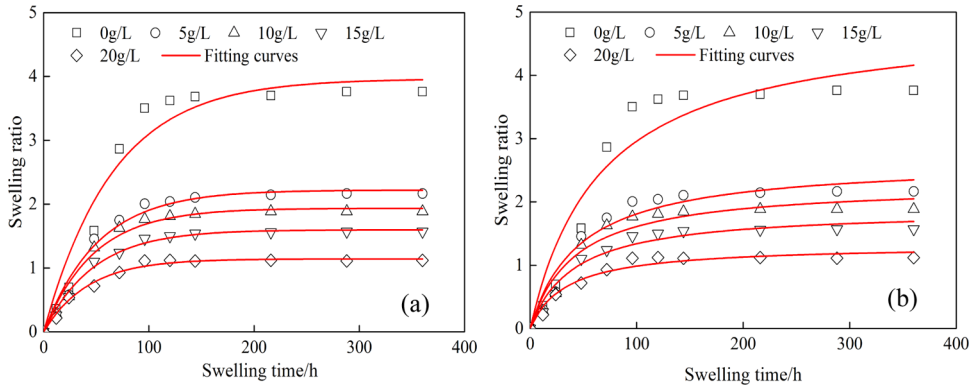

Figure 12. Fitted curves of the swelling experimental data at various salinities: (a) first-order kinetics model; and (b) second-order kinetics model.

A plot of the equilibrium swelling ratio versus temperature is shown in Figure 10b. The equilibrium swelling ratio gradually increases with increasing temperature. The plot shows that the relationship between the equilibrium swelling ratio and temperature can also be approximated by the following exponential form

$$Q_e = a_T \cdot \exp(b_T \cdot T) \tag{4}$$

where a_T and b_T are the fitted parameters and T is the temperature, °C. Under these experimental conditions, parameters a_T and b_T could be determined to be 1.0210 and 0.0152, respectively, by nonlinear regression analysis with correlation coefficient (R^2 = 0.998).

Thus, the effects of salinity and temperature on the equilibrium swelling ratio are described as an exponential form. Then, the simultaneous effect of salinity and temperature on the equilibrium swelling ratio can be expressed as follows

$$\ln Q_e = a + b \cdot C + c \cdot T \tag{5}$$

where a, b, and c are the fitted parameters. A multivariate statistical analysis of the experimental data was carried out to obtain these fitted parameters by fitting the experimental data to eq 5 using MATLAB software. Figure 11a shows a fitted surface of the equilibrium swelling ratio versus salinity and temperature. Parameters a, b, and c are 0.767, −0.0701, and 0.0136, respectively, using multivariate statistical analysis with correlation coefficient (R^2 = 0.969). The negative value of b and the positive value of c indicate that decreasing salinity and increasing temperature are beneficial to the swelling, which is in agreement with the experimental results. The equilibrium swelling ratio at T = 0 °C and C = 0 g/L can be obtained by the value of a.

Based on the fitting results of eq 5, the isograms of the equilibrium swelling ratio versus salinity and temperature are plotted in Figure 11b. With the change of salinity, the distribution of isograms at high temperature is more intensive than at low temperature, which illustrates that salinity has a greater impact on equilibrium swelling ratio. In addition, with the change of temperature, the distribution of isograms at low salinity is more intensive than at high salinity, which suggests that temperature has a greater effect on equilibrium swelling ratio. The results obtained from eq 5 are consistent with the result from eq 2 and prove that eq 5 is correct within the experimental conditions.

4.3. Swelling Kinetics Analysis. Swelling experimental data were analyzed using the first-order and second-order kinetics models to better understand the swelling controlling mechanism and investigate the swelling kinetics. The differential form of a first-order kinetics model is written as follows

$$\frac{dQ}{dt} = k_1(Q_e - Q) \tag{6}$$

where t is the swelling time, h, Q is the swelling ratio at time t, and k_1 is the swelling rate constant of first-order, h^{-1}. The nonlinear form of a first-order kinetics model obtained by integrating eq 6 with respect to time t is expressed as follows

$$Q = Q_e(1 - e^{-k_1 t}) \tag{7}$$

DOI: 10.1021/acs.energyfuels.9b00131
Energy Fuels 2019, 33, 3077−3088

with the differential form of second-order kinetics model written as follows

$$\frac{dQ}{dt} = k_2(Q_e - Q)^2 \quad (8)$$

where k_2 is the swelling rate constant of the second-order, h^{-1}. The nonlinear form of the second-order kinetics model obtained by integrating eq 8 with respect to time t is expressed as follows

$$Q = \frac{k_2 Q_e^2 t}{1 + k_2 Q_e t} \quad (9)$$

The fitted curves of the swelling experimental data at various salinities, calculated by the first-order and second-order kinetics models, are shown in Figure 12, and their fitted parameters are shown in Table 2. The fitted curves in Figure 12 show that the experimental data at different salinities are fitted by the first-order kinetics model that is more suitable than the second-order kinetics model. According to Table 2, the correlation coefficients (R^2) of the first-order kinetics model are higher than those of the second-order kinetics model at same salinity. These results suggest that the swelling process of SiO_2/P(MBAAm-*co*-AM) composite nanoparticles could be better described by the first-order kinetics model. In addition, the equilibrium swelling ratios calculated by the first-order and second-order kinetics models at various salinities are shown in Figure 13, compared with the experimental data. As seen in Figure 13, the calculated Q_e values of the first-order kinetics model are closer to the experimental values than those of the second-order kinetics model, which indicates that the swelling mechanism of SiO_2/P(MBAAm-*co*-AM) composite nanoparticles obeys the first-order kinetics model. Based on the assumption of first-order kinetics, it can be inferred that the rate-limiting step in the adsorption of water is physical adsorption during the swelling process.

Table 2. Fitted Parameters of the Swelling Experimental Data at Various Salinities

	first-order kinetics model			second-order kinetics model		
salinity (g/L)	Q_e	k_1	R^2	Q_e	k_2	R^2
0	3.966	0.0152	0.951	4.928	0.00305	0.918
5	2.221	0.0195	0.978	2.650	0.00814	0.948
10	1.936	0.0211	0.978	2.289	0.0104	0.944
15	1.599	0.0212	0.989	1.882	0.0131	0.962
20	1.143	0.0239	0.987	1.320	0.0223	0.959

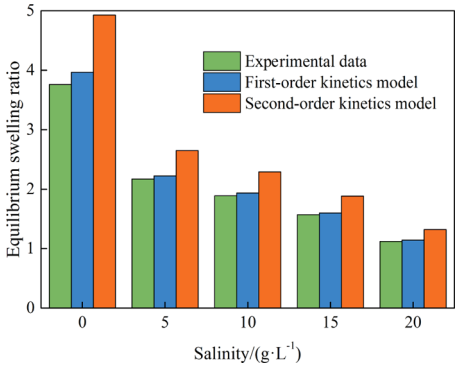

Figure 13. Comparison of the calculated Q_e values with the experimental data at various salinities.

Similarly, the fitted curves of the swelling experimental data at various temperatures, calculated by first-order and second-order kinetics models, are shown in Figure 14, and their fitted parameters are shown in Table 3. According to Figure 14, the fitted curves show the experimental data fit the first-order kinetics model at temperatures less than 60 °C, whereas they fit the second-order kinetics model at temperatures exceeding 60 °C. According to Table 3, the correlation coefficients (R^2) of the first-order kinetics model are higher at temperatures less than 60 °C, whereas the correlation coefficients (R^2) of the second-order kinetics model are higher at temperatures exceeding 60 °C. However, as seen in Figure 15, which shows the comparison of equilibrium swelling ratios calculated by the first-order and second-order kinetics models with the experimental data at various temperatures, the calculated Q_e values of the first-order kinetics model are still closer to the experimental values at temperatures from 30 to 70 °C. Therefore, the swelling mechanism of SiO_2/P(MBAAm-*co*-AM) composite nanoparticles obeys the first-order kinetics model.

Activation energy of the swelling process of SiO_2/P(MBAAm-*co*-AM) composite nanoparticles in an aqueous solution is analyzed for swelling rate constants at various temperatures using Arrhenius's equation as follows

$$k = A\, e^{-E_a/RT} \quad (10)$$

or

$$\ln k = -\frac{E_a}{RT} + \ln A \quad (11)$$

where k is the swelling rate constant, A is the frequency factor, E_a is the apparent activation energy, kJ/mol, T is the absolute temperature, K, and R is the ideal gas constant, 8.314 J/(mol K).

The values of E_a were calculated from the slope of the plot of $\ln k$ versus T^{-1}. The fitted curves of the swelling rate constants obtained by first-order and second-order kinetics models at various temperatures are shown in Figure 16. According to Figure 16, the E_a values of the first-order and second-order kinetics models are calculated to be 16.17 kJ/mol with the correlation coefficient (R^2 = 0.947) and 14.07 kJ/mol with the correlation coefficient (R^2 = 0.802), respectively. The E_a values of the two models are close to each other, but the correlation coefficient of the first-order kinetics model is higher than that of the second-order kinetics model. Consequently, this result further proves that the swelling mechanism of SiO_2/P(MBAAm-*co*-AM) polymeric nanoparticles obeys the first-order kinetics model.

4.4. Swelling Thermodynamics Analysis. The swelling process of SiO_2/P(MBAAm-*co*-AM) composite nanoparticles in an aqueous solution was analyzed for swelling ratios at various temperatures using the Van't Hoff's equation as follows

$$\ln K = -\frac{\Delta H^\theta}{RT} + \frac{\Delta S^\theta}{R} \quad (12)$$

$$K = Q_e/C_e \quad (13)$$

$$\Delta G^\theta = \Delta H^\theta - T\Delta S^\theta \quad (14)$$

where K is the swelling equilibrium constant, ΔH^θ is the enthalpy change, J/mol, ΔS^θ is the entropy change, J/(mol K),

DOI: 10.1021/acs.energyfuels.9b00131
Energy Fuels 2019, 33, 3077−3088

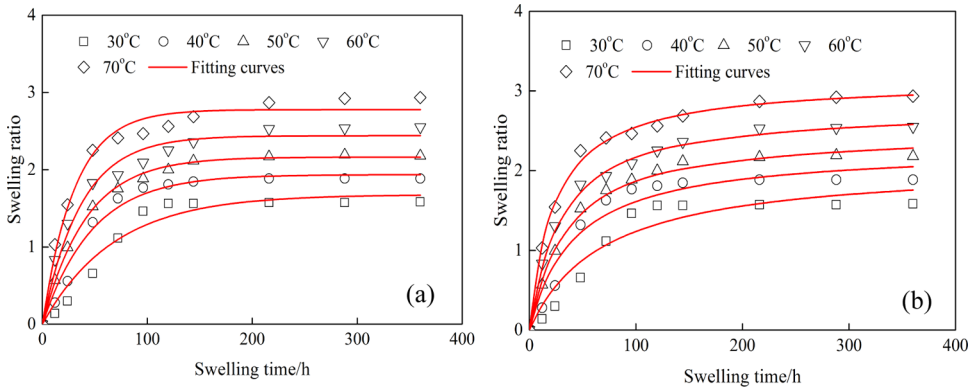

Figure 14. Fitted curves of the swelling experimental data at various temperatures: (a) first-order kinetics model and (b) second-order kinetics model.

Table 3. Fitted Parameters of the Swelling Experimental Data at Various Temperatures

temperature (°C)	first-order kinetics model			second-order kinetics model		
	Q_e	k_1	R^2	Q_e	k_2	R^2
30	1.678	0.0147	0.951	2.096	0.00687	0.918
40	1.936	0.0211	0.978	2.289	0.0104	0.944
50	2.163	0.0243	0.997	2.491	0.0122	0.992
60	2.440	0.0274	0.977	2.778	0.0130	0.997
70	2.777	0.0327	0.981	3.139	0.0137	0.996

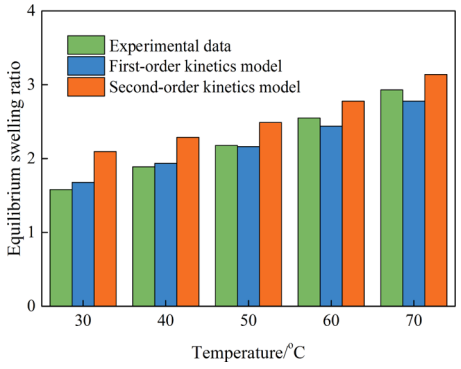

Figure 15. Comparison of the calculated Q_e values with the experimental data at various temperatures.

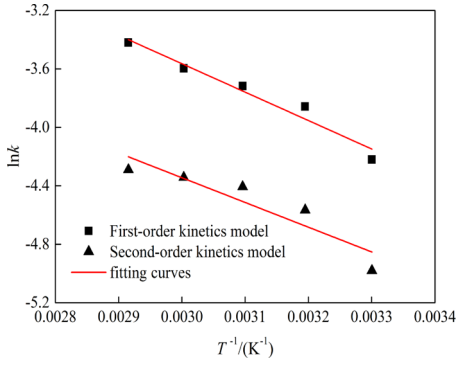

Figure 16. Arrhenius plots of the swelling process of SiO_2/P(MBAAm-*co*-AM) composite nanoparticles.

and ΔG^{θ} is the free enthalpy, kJ/mol. The values of thermodynamic parameters were obtained from the slope and intercept of the plot of ln K versus T^{-1}. The fitted curves of the swelling ratios at various temperatures are shown in Figure 17. The values of parameters are recorded in Table 4.

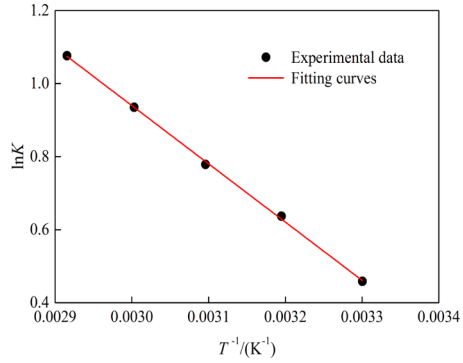

Figure 17. Van't Hoff plot of the swelling process.

Table 4. Thermodynamic Parameters of the Swelling Process

T (°C)	K	ΔG^{θ} (kJ/mol)	ΔH^{θ} (kJ/mol)	ΔS^{θ} (J/(mol K))
30	1.582	−1.161	13.257	47.584
40	1.891	−1.637		
50	2.179	−2.113		
60	2.548	−2.588		
70	2.934	−3.064		

The positive value of ΔH^{θ} indicates that the swelling process of SiO_2/P(MBAAm-*co*-AM) composite nanoparticles is endothermic. The swelling process is essentially a process of adsorbing water, which can be explained by the adsorption theory.[44,45] It has been reported that in adsorption process, the value of ΔH^{θ} from 2.1 to 20.9 kJ/mol is indicative of physical adsorption, whereas that from 20.9 to 418.4 kJ/mol is indicative of chemical adsorption.[36] The ΔH^{θ} value (13.257 kJ/mol) in this study illustrates that physical adsorption plays a significant role in the swelling process. The positive value of ΔS^{θ} (47.584 J/(mol K)) indicates an increase of randomness at the interface between nanoparticle and solution during the swelling process. Besides, the negative values of ΔG^{θ} at temperatures from 30 to 70 °C show that the swelling process of SiO_2/P(MBAAm-*co*-AM) composite nanoparticles is spontaneous. The decreased ΔG^{θ} values with increasing temperature demonstrate that it is more beneficial for the swelling process at higher temperatures.

DOI: 10.1021/acs.energyfuels.9b00131
Energy Fuels 2019, 33, 3077−3088

5. CONCLUSIONS

In this study, SiO_2/P(MBAAm-*co*-AM) polymeric nanoparticles were successfully prepared by distillation precipitation polymerization. SiO_2/P(MBAAm-*co*-AM) polymeric nanoparticles exhibit a good swelling property in an aqueous solution at high salinity under low-temperature conditions. Decrease in salinity and increase in temperature both can increase the swelling ratio of SiO_2/P(MBAAm-*co*-AM) composite nanoparticles, which can reasonably be explained by the Flory theory. The core-flooding experiments demonstrate that the suspension of SiO_2/P(MBAAm-*co*-AM) polymeric nanoparticles can improve EOR via enlarging swept volume to recover more residual oil in cores. SiO_2/P(MBAAm-*co*-AM) suspension can improve oil recovery from 10.28 to 21.97% with an increase of particle size from 580 to 1160 nm.

The equilibrium swelling ratio is one of the most important parameters for swelling properties. The relationship formula of the equilibrium swelling ratio with salinity and temperature has been established, which is consistent with the Flory theory. The kinetic result indicates that the first-order kinetics model is the best fit to the swelling process. The thermodynamic parameters demonstrate that the swelling process of SiO_2/P(MBAAm-*co*-AM) polymeric nanoparticles is spontaneous and endothermic in nature. The swelling of SiO_2/P(MBAAm-*co*-AM) is controlled by physical adsorption involving the diffusion of water molecules.

AUTHOR INFORMATION

Corresponding Authors

*E-mail: longyunqian@163.com (Y.L.).
*E-mail: huangxh@zjou.edu.cn (X.H.).

ORCID

Yunqian Long: 0000-0002-5176-3484

Notes

The authors declare no competing financial interest.

ACKNOWLEDGMENTS

We gratefully acknowledge the financial support from the Natural Science Foundation of Zhejiang Province (Project No. LY19A020004), the National Natural Science Foundation of China (Project Nos. 11602221 and 11472246), the General Research Projects of Zhejiang Provincial Department of Education (Project No. Y201840296), and the Cultivation Project of Zhejiang Ocean University.

REFERENCES

(1) Fan, T.-Y.; Song, X.-M.; Wu, S.-H.; Li, Q.-Y.; Wang, B.-H.; Li, X.-B.; Li, H.; Liu, H.-L. *Petro. Explor. Dev.* **2015**, *42*, 541−547.
(2) Han, Y.-J.; Zhou, C.-C.; Yu, J.; Li, C.-L.; Hu, F.-L.; Xu, H.-J.; Yuan, C. *Fuel* **2019**, *239*, 1246−1257.
(3) Alhuraishawy, A. K.; Bai, B.-J.; Wei, M.-Z.; Geng, J.-M.; Pu, J.-Y. *Fuel* **2018**, *220*, 898−907.
(4) Wang, J.-L.; Song, H.-Q.; Rasouli, V.; Killough, J. *J. Pet. Sci. Eng.* **2019**, *173*, 237−245.
(5) Bell, D.; Kane, I. A.; Pontén, A. S.; Flint, S. S.; Hodgson, D. M.; Barrett, B. J. *Mar. Pet. Geol.* **2018**, *98*, 97−115.
(6) Song, H.-Q.; Yu, M.-X.; Zhu, W.-Y.; Wu, P.; Lou, Y.; Wang, Y.-H.; Killough, J. *Int. J. Heat Mass Transfer* **2015**, *80*, 626−635.
(7) Chu, H.-Q.; Han, W.-W.; Cao, W.-J.; Gu, M.-Y.; Xu, G.-J. *Energy* **2019**, *166*, 392−400.
(8) Xu, P.; Qiu, S.-X.; Cai, J.-C.; Li, C.-H.; Liu, H.-C. *J. Power Sources* **2017**, *362*, 73−79.
(9) Guo, Z.-Q.; Dong, M.-Z.; Chen, Z.-G.; Yao, J. *J. Pet. Sci. Eng.* **2013**, *112*, 335−340.
(10) Bahrami, P.; Kazemi, P.; Mahdavi, S.; Ghobadi, H. *Fuel* **2016**, *179*, 289−298.
(11) Delshad, M.; Han, C.-Y.; Veedu, F. K.; Pope, G. A. *J. Pet. Sci. Eng.* **2013**, *108*, 1−9.
(12) Soleimani, H.; Baig, M. K.; Yahya, N.; Khodapanah, L.; Sabet, M.; Demiral, B. M.; Burda, M. *Results Phys.* **2018**, *9*, 39−48.
(13) Gbadamosi, A. O.; Junin, R.; Manana, M. A.; Yekeen, N.; Agi, A.; Oseh, J. O. *J. Ind. Eng. Chem.* **2018**, *66*, 1−19.
(14) Yuan, B.; Moghanloo, R. G.; Wang, W.-D. *Fuel* **2018**, *215*, 474−483.
(15) Han, H.-Y.; Li, T.-X.; Song, H.-Q.; Wang, Y.-H.; Killough, J. *Int. J. Oil, Gas Coal Technol.* **2017**, *15*, 47−59.
(16) Moradi, B.; Pourafshary, P.; Jalali, F.; Mohammadi, M.; Emadi, M. A. *J. Nat. Gas Sci. Eng.* **2015**, *27*, 64−73.
(17) Nwidee, L. N.; Al-Anssari, S.; Barifcani, A.; Sarmadivaleh, M.; Lebedev, M.; Iglauer, S. *J. Pet. Sci. Eng.* **2017**, *149*, 782−788.
(18) Ehtesabi, H.; Ahadian, M. M.; Taghikhani, V.; Ghazanfari, M. H. *Energy Fuels* **2014**, *28*, 423−430.
(19) Bayat, A. E.; Junin, R.; Samsuri, A.; Piroozian, A.; Hokmabadi, M. *Energy Fuels* **2014**, *28*, 6255−6266.
(20) Al-Anssari, S.; Barifcani, A.; Wang, S.-B.; Maxim, L.; Iglauer, S. *J. Colloid Interface Sci.* **2016**, *461*, 435−442.
(21) Hendraningrat, L.; Li, S.-D.; Torsæter, O. *J. Pet. Sci. Eng.* **2013**, *111*, 128−138.
(22) Radnia, H.; Rashidi, A.; Nazar, A. S.; Eskandari, M. M.; Jalilian, M. *J. Mol. Liq.* **2018**, *271*, 795−806.
(23) Bagherpour, S.; Rashidi, A.; Mousavi, S. H.; Izadi, N.; Hamidpour, E. *Colloids Surf., A* **2019**, *563*, 37−49.
(24) Pu, W.-F.; Liu, R.; Wang, K.-F.; Li, K.-X.; Yan, Z.-P.; Li, B.; Zhao, L. *Ind. Eng. Chem. Res.* **2015**, *54*, 798−807.
(25) Ponnapati, R.; Karazincir, O.; Dao, E.; Ng, R.; Mohanty, K. K.; Krishnamoorti, R. *Ind. Eng. Chem. Res.* **2011**, *50*, 13030−13036.
(26) Cheng, Y.-M.; Zhao, M.-Y.; Zheng, C.; Guo, S.; Li, X.-H.; Zhang, Z.-J. *Energy Fuels* **2017**, *31*, 6345−6351.
(27) Gu, M.-Y.; Chen, X.; Wu, C.-C.; He, X.-H.; Chu, H.-Q.; Liu, F.-S. *Energy Fuels* **2017**, *31*, 5571−5580.
(28) Song, H.-Q.; Cao, Y.; Yu, M.-X.; Wang, Y.-H.; Killough, J.; Leung, J. *J. Nat. Gas Sci. Eng.* **2015**, *22*, 172−181.
(29) Wang, L.; Zhang, G.-C.; Ge, J.-J.; Li, G.-H.; Zhang, J.-Q.; Ding, B.-D. In *Preparation of Microgel Nanospheres and Their Application in EOR*, Proceedings of the CPS/SPE International Oil & Gas Conference and Exhibition; Beijing, China, June 8−10, 2010.
(30) Hu, Z.-L.; Haruna, M.; Gao, H.; Nourafkan, E.; Wen, D.-S. *Ind. Eng. Chem. Res.* **2017**, *56*, 3456−3463.
(31) Zhu, D.; Gao, P.-J.; Yagi, N.; Schumacher, H. *Int. J. Hypertens.* **2014**, *2014*, 1−11.
(32) Alaskar, M.; Ames, M.; Connor, S.; Lui, C.; Cui, Y.; Li, K.-W.; Horne, R. N. In *Nanoparticle and Microparticle Flow in Porous and Fractured Media: An Experimental Study*, Proceedings of the SPE Annual Technical Conference and Exhibition; Denver, CO, Oct 30−Nov 2, 2011.
(33) Liu, R.; Pu, W.-F.; Du, D.-J. *J. Ind. Eng. Chem.* **2017**, *46*, 80−90.
(34) Tian, H.; Liu, J.; O'Donnell, K.; Liu, T.-T.; Liu, X.-M.; Yan, Z.-F.; Liu, S.-M.; Jaroniec, M. *J. Colloid Interface Sci.* **2016**, *476*, 55−61.
(35) Effati, E.; Pourabbas, B. *Powder Technol.* **2013**, *246*, 473−477.
(36) Huang, Q.; Liu, M.-Y.; Mao, L.-C.; Xu, D.-Z.; Zeng, G.-J.; Huang, H.-Y.; Jiang, R.-M.; Deng, F.-J.; Zhang, X.-Y.; Wei, F. *J. Colloid Interface Sci.* **2017**, *499*, 170−179.
(37) Liu, H.-S.; Jiang, Y.-G.; Liu, D.-D.; Li, S.-D.; Yang, X.; Ji, Y.-Q.; Cui, Y.-P. *Vib. Spectrosc.* **2018**, *96*, 101−105.
(38) Maiti, K. S. *Chem. Phys.* **2018**, *515*, 509−512.
(39) Fan, Z.-S.; Chen, J.-B.; Guo, W.-J.; Ma, F.; Sun, S.-Q.; Zhou, Q. *J. Mol. Struct.* **2018**, *1164*, 297−302.
(40) Madathingal, R. R.; Wunder, S. L. *Thermochim. Acta* **2011**, *526*, 83−89.
(41) Toledo-Fuentes, X.; Molinaro, C.; Cecchet, F. *Colloids Surf., B* **2018**, *172*, 254−261.

DOI: 10.1021/acs.energyfuels.9b00131
Energy Fuels 2019, 33, 3077−3088

(42) Zhang, Z.-P.; Rong, M.-Z.; Zhang, M.-Q. *Prog. Polym. Sci.* **2018**, *80*, 39−93.
(43) Flory, P. J. *Principles of Polymer Chemistry*; Cornell University Press: New York, 1953.
(44) Dixit, A.; Bag, D. S.; Kalra, S. J. S. *Polymer* **2017**, *119*, 263−273.
(45) Mao, J.; Abushammala, H.; Pereira, L. B.; Laborie, M.-P. *Carbohydr. Polym.* **2016**, *153*, 284−291.

DOI: 10.1021/acs.energyfuels.9b00131
Energy Fuels 2019, 33, 3077−3088